RSC Advances

PAPER

View Article Online
View Journal | View Issue

Cite this: *RSC Adv.*, 2018, **8**, 38621

Structural characterization and magnetic properties of undoped and copper-doped cobalt ferrite nanoparticles prepared by the octanoate coprecipitation route at very low dopant concentrations

Hypolite Mathias Kamta Tedjieukeng,*[a] Patrice Kenfack Tsobnang,[b] Roussin Lontio Fomekong,[a] Ekane Peter Etape,[c] Pattayil A. Joy,[d] Arnaud Delcorte[e] and John Ngolui Lambi[a]

Nanoparticles of undoped and copper-doped cobalt ferrite $Co_{1-x}Cu_xFe_2O_4$ at very low dopant concentrations (x = 0; 0.02; 0.04; 0.06; 0.08) were successfully synthesized by pyrolysis of the corresponding hetero metal octanoate precursors obtained *via* coprecipitation using the octanoate ligand as precipitating agent. The precursors were then characterized by FTIR, ICP-AES and TG-DTA analyses and the results reveal the formation of a copper-cobalt-iron hydroxooctanoate represented by the formula $[Co_{1-x}Cu_xFe_2(C_8H_{15}O_2)_6(OH)_2{\cdot}2H_2O]$. The decomposition products obtained upon pyrolysis in air at 400 °C for 3 h were characterized by FTIR, XRD, SEM, TEM, XPS and VSM analyses. FTIR and XRD analyses showed the formation of a single phase mixed spinel ferrite while TEM analysis showed that the particles have a spherical shape with a mean size of 20 nm and form spherical agglomerates with sizes reaching 500 nm in some cases as the SEM images show. The chemical states of the metallic species in the samples were revealed by XPS to be Cu^{2+}, Co^{2+} and Fe^{3+}. These results combined with XRD confirmed the mixed spinel structure, $Co_{1-x}Cu_xFe_2O_4$ in which Cu^{2+} ions substitute Co^{2+} ions in tetrahedral sites for x lower than 0.06 and in octahedral sites for x between 0.06 and 0.08. Magnetic parameters such as saturation magnetization (M_s), coercivity (H_c), remanent magnetization (M_r), magnetocrystalline anisotropy constant (K) and reduced magnetization (M_r/M_s), obtained from magnetic hysteresis loops measured at room temperature, are in agreement with this mixed spinel structure and also indicate that these materials are ferromagnetic and could be good candidates for applications in biomedicine and in microwave devices.

Received 15th October 2018
Accepted 10th November 2018

DOI: 10.1039/c8ra08532c

rsc.li/rsc-advances

1. Introduction

Magnetic spinel ferrite nanomaterials have nowadays attracted a lot of interest because of the important roles they play in enhancing knowledge and understanding of the functioning of magnetic materials in general and ferrites in particular.[1–4] This is more so given the fact that ferrites have several technological applications such as in high density magnetic storage, sensors, biomedical drug delivery, broadband transformers, computer circuitry, carrier telephony and highly efficient catalysts.[5–11] Most of these applications depend on the magnetic properties of these materials which could be ascribed to a complex interplay of several factors where cationic distribution and spin canting are fundamental and predominant.[12]

The general formula for spinel ferrites is MFe_2O_4, where M is a divalent metal ion and Fe is present in the +3 oxidation state.[13–16] Generally, there are two types of ferrite spinel structures: the normal and the inverse, even though most spinel ferrites are inverse.[17,18] In the normal spinel, the tetrahedral sites occupied contain the M^{2+} ions while the Fe^{3+} ions are located in the octahedral sites occupied.[19–21] In the inverse spinel, however, all the M^{2+} ions and half of the Fe^{3+} ions are located in the octahedral sites occupied, with the other half of the Fe^{3+} ions in the tetrahedral sites occupied. This implies that the cation distribution between the two interstitial sites could influence the magnetic properties of the spinel ferrites.[18]

[a]*Materials Chemistry Laboratory, Department of Chemistry, Higher Teacher Training College, University of Yaoundé I, P. O. Box 47, Yaoundé, Cameroon*

[b]*Department of Chemistry, University of Dschang, P. O. Box 67, Dschang, Cameroon*

[c]*Department of Chemistry, Faulty of Science, University of Buea, P. O. Box 63, Buea, Cameroon*

[d]*Physical Chemistry Division, National Chemical Laboratory, Pune 411008, India*

[e]*Pole Bio & Soft Mater, Institut de la Matière Condensée et des Nanosciences, Université Catholique de Louvain, Croix du Sud 1, 1348, Louvain-La-Neuve, Belgium*

The cobalt ferrite spinel ($CoFe_2O_4$), in particular, is a hard magnetic material with well-known properties such as mechanical hardness, remarkable chemical stability, high anisotropy ($K_a = 3 \times 10^5$ J m^{-3})[8] and a relatively high saturation magnetization (M_s) and coercivity (H_c). As a result, it has many applications such as in ferrofluids technology, as biocompatible magnetic nanoparticles for cancer treatment, for magnetic resonance imaging and in microwave devices.[5,22–25] The substitution of cobalt by copper in $CoFe_2O_4$ is known to modify the structural and magnetic properties of the material making it a suitable candidate for some applications like in biomedical drug delivery and in microwave, switching and memory devices.[10,26]

Most often, the magnetic properties of cobalt ferrite spinels depend on the preparation method[27–29] and the nature of the dopant used.[30,31] Ma *et al.*[28] synthesized the cobalt ferrite ($CoFe_2O_4$) by the solvothermal method at 160 °C and obtained a saturation magnetization of 73 emu g^{-1} while Gopalan *et al.*[29] obtained a saturation magnetization of 48 emu g^{-1} for the same material synthesized by sol–gel combustion method. Prathapani *et al.*[30] synthesized $CoFe_{2-x}Er_xO_4$ ferrite nanoparticles (with $x = 0$, 0.01, 0.02, 0.03 and 0.04) by the sol–gel assisted auto combustion method. For $x = 0$, they obtained a magnetization (M) of 72.1 emu g^{-1} at room temperature. As x increased from 0.01 to 0.02 this value increased to 75.3 emu g^{-1} while as x increased from 0.03 to 0.04 the value decreased to 73.2 emu g^{-1}. Tholkappiyan *et al.*[31] synthesized $MgFe_{2-x}Er_xO_4$ ferrite nanoparticles (with $x = 0$, 0.02, 0.04 and 0.06) by combustion method and showed that at room temperature, the saturation magnetization (M_s) increased from 13.2 emu g^{-1} for $x = 0$ to 44.1 emu g^{-1} for $x = 0.06$.

Several methods[6,7,22–24,26,32,33] have been used to synthesize nano-structured mixed copper-cobalt ferrites. These methods include the microwave assisted sol–gel,[6] co-precipitation,[7,24] sol–gel,[22,23] ceramic,[26] microemulsion[32] and soft chemistry methods.[33] Among all these methods, coprecipitation has been preferred. It involves precipitating simultaneously two or more metal salts in solution by using a precipitating agent (or ligand) and subsequently thermally decomposing the precipitate.[34] Relative to the other methods, it offers several advantages such as better distribution of the constituents in the resulting ferrites, low operating temperature, low cost and good control of stoichiometry.[7,35] Many studies[10,24,36] have reported on high amounts of substitution, where an increase in Cu content has resulted in a decrease in the magnetization. For example, Jnaneshwara *et al.*[10] synthesized $Co_{1-x}Cu_xFe_2O_4$ (with $x = 0$, 0.1, 0.2, 0.3, 0.4, 0.5) by the solution combustion method and showed that the saturation magnetization decreased from 38.5 to 26.7 emu g^{-1} as the concentration of Cu^{2+} increased. Balavijayalakshmi *et al.*,[24] on the other hand, synthesized $Co_{1-x}Cu_xFe_2O_4$ nanoparticles ($x = 0$, 0.2, 0.4, 0.6, 0.8, 1) by coprecipitation method followed by sintering at 900 °C while Samavati *et al.*[36] obtained the same material ($x = 0$, 0.3, 0.5, 0.7, 1) by the same method with sintering at 800 °C. Their results showed that when the copper concentrations increased, the saturation magnetization (M_s) decreased from 72.06 emu g^{-1} to 21.11 emu g^{-1} for the former and from 61.06 to 39.52 emu g^{-1} for the latter. From all what precedes, it is evident that the preparation method and sometimes the sintering temperature influence either the size or the morphology of the spinel ferrite nanomaterial, which in turn, influences the magnetic properties.

In this paper, we therefore report for the first time and to the best of our knowledge, a controlled synthesis of $Co_{1-x}Cu_xFe_2O_4$ ferrite nanoparticles at very low dopant concentrations ($x = 0$, 0.02, 0.04, 0.06, 0.08) by a simple but versatile method which involves the pyrolysis of the precursors obtained by a coprecipitation route using aqueous solutions of the octanoate ligand as precipitating agent. The use of octanoate as precipitating agent and the interval of the dopant applied in this synthesis could certainly have an influence on the magnetic properties of the as-synthesized materials. The precursors were characterized by elemental (C, H, N) analyses, ICP-AES, FTIR and TGA. The decomposition products, obtained from thermal decomposition of the precursors, were characterized by FTIR, XRD, TEM, SEM, XPS and VSM.

2. Experimental section

2.1. Synthesis procedure

Copper chloride ($CuCl_2 \cdot 2H_2O$), cobalt nitrate [$Co(NO_3)_2 \cdot 6H_2O$], ferric nitrate [$Fe(NO_3)_3 \cdot 9H_2O$], lithium hydroxide ($LiOH \cdot H_2O$) and octanoic acid, all obtained from Aldrich, were used without further purification.

The undoped and copper-doped cobalt ferrite nanoparticles, $Co_{1-x}Cu_xFe_2O_4$ ($x = 0$, 0.02, 0.04, 0.06, 0.08) were obtained *via* two experimental steps: the precursors were first synthesized by coprecipitation in aqueous solution containing iron, copper and cobalt ions in the right ratio using the octanoate ligand as precipitating agent then followed by thermal decomposition of the precursors obtained. For example, for the synthesis of cobalt iron octanoate precursor: lithium octanoate was first prepared in aqueous solution by adding lithium hydroxide (13 mmol) to octanoic acid (13 mmol). After a few minutes, an aqueous solution containing cobalt(II) nitrate (1.6 mmol) and iron(III) nitrate (3.2 mmol) was poured drop by drop into the previously prepared solution of lithium octanoate with continuous stirring. The resulting brown solution was then stirred for another 1 h at room temperature (30 °C). The resulting precipitate (cobalt-iron octanoate) was then filtered (to remove the $LiNO_3$), washed with ethanol and dried in a desiccator for two days at room temperature to obtain a light brown powder. The as-prepared precursor powder was decomposed in air at 400 °C in a tubular furnace (heating rate 15 °C min^{-1}) for 3 h. The scheme of the synthesis is shown in Fig. 1. The as-prepared powder samples of $Co_{1-x}Cu_xFe_2O_4$ for $x = 0$, 0.02, 0.04, 0.06, and 0.08 were labelled, respectively, as S1, S2, S3, S4 and S5 while the corresponding decomposed products were labelled as S1P, S2P, S3P, S4P, and S5P.

2.2. Characterization methods

The metal contents of the precursors were estimated by Inductively Coupled Plasma Atomic Emission Spectroscopy (ICP-AES) using a Thermo Jarrell Ash Iris Advantage apparatus.

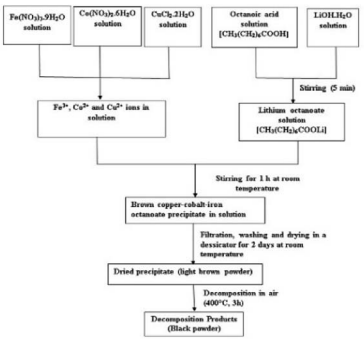

Fig. 1 Flow chart for synthesis of $Co_{1-x}Cu_xFe_2O_4$ nanoparticles using co-precipitation method.

The solution used for measurements was obtained as follows. A few milligrams (~80 mg) of the sample were digested in 4 mL of mixed acid (3 mL of concentrated nitric acid + 1 mL of concentrated hydrochloric acid) and the resulting solution was diluted to 1000 mL using distilled water. A LECO CHN 900 Elemental Analyzer was used for the C and H analyses in the precursors. The functional groups of the octanoate ligand were determined using Fourier Transform Infra-Red (FTIR) spectroscopy using a Quick Lock Single Reflection Horizontal ATR Accessory from Bruker. The thermal decomposition behaviour of the precursors was studied by Thermogravimetric Analysis (TGA) on a METTLER TOLEDO Thermal Analyzer in air at a flow rate of 100 mL min^{-1}, between 25–900 °C and at a heating rate of 10 °C min^{-1}. Powder X-Ray Diffraction (XRD) data of the decomposed products were collected at room temperature on a D5000 Siemens Kristalloflex θ–2θ powder diffractometer which has a Bragg–Brentano geometry, is equipped with a graphite-monochromated Cu-Kα (λ = 1.54056 Å) radiation. For the experiment, the samples were spread out on a flat silicon plate in such a manner as to avoid preferred orientations. The patterns were recorded in the range of 5–90° with a scan step of 0.02° (2θ) and a 2 s acquisition interval. The XRD patterns were compared to those of the $CoFe_2O_4$ patterns of the ICCD using the High-Score Plus software for phase identification. The recorded patterns were also indexed and the unit cell refined by using the FULLPROF suite program. The morphology of the powder was determined by Scanning Electron Microscopy (SEM) using a high resolution FEG JEOL7600F with an accelerating voltage of 1 kV. The morphologies of the samples were confirmed by Transmission Electron Microscopy (TEM, Leo922 Model from Zeiss) at an accelerating voltage of 120 kV. The TEM samples were prepared by dropping a sonicated water dispersion of the powder samples on a carbon-coated copper grid. The composition, the chemical state of the various constituents and the stoichiometry of each sample were determined by X-ray Photoelectron Spectroscopy (XPS) using a Kratos Axis Ultra spectrometer (Kratos Analytical, Manchester, UK) equipped with a monochromatized aluminum X-ray source (powered at 10 mA and 15 kV) and an eight-channeltron detector. The magnetic measurements were carried out at room temperature a SQUID-Vibrating Sample Magnetometer (Quantum Design) with an applied field in the range ± 60 kOe.

3. Results and discussions

3.1. Characterization of precursors

3.1.1. Elemental analysis. The metal contents of all the precursor samples and the C and H contents of the two samples S1 and S5, selected as representative of the five samples, are reported in Table 1. The results obtained are compatible with a copper-cobalt-iron hydroxooctanoate with general formula $Co_{1-x}Cu_xFe_2(C_8H_{15}O_2)_6(OH)_2\cdot 2H_2O$ (x = 0, 0.02, 0.04, 0.06, 0.08).

3.1.2. FTIR analysis. Fig. 2 shows the FTIR spectra of the five samples (S1 to S5) while the characteristic bands of these samples and their assignments are as presented in Table 2. The absence of free carbonyl [ν(C=O)] vibration around 1700 cm^{-1} is an indication that the entire carboxylate group is engaged in the coordination bond. Lambi *et al.*[37] and Mesubi *et al.*[38] have shown that when the value of the separation between the bands, $\Delta\nu$ ($=\nu COO_{asym} - \nu COO_{sym}$) is above 200 cm^{-1}, a monodentate mode of bonding between the carboxylate group (COO^-) of the ligand and the metal atoms is indicated, a value of $\Delta\nu$ below 110 cm^{-1} is attributable to the chelating bidentate mode while $\Delta\nu$ between 140 cm^{-1} and 200 cm^{-1} is attributed to the bridged bidentate bonding mode.[39] All the samples investigated (S1 to S5) showed $\Delta\nu$ values of 150 cm^{-1} corresponding to the bridged bidentate bonding mode of the octanoic acid to the metals These FTIR results are in good agreement with those reported on iron carboxylate complexes.[40,41]

Table 1 Metal, C and H contents of the precursors[a]

	Elemental contents (%)									
	Fe		Co		Cu		C		H	
Samples	Theo*	Exp**	Theo	Exp	Theo	Exp	Theo	Exp	Theo	Exp
S1	10.2	9.6	5.4	3.4	0	0	52.41	53.12	8.80	8.58
S2	10.2	9.4	5.3	3.6	0.12	0.13	—	—	—	—
S3	10.2	9.6	5.1	3.4	0.23	0.20	—	—	—	—
S4	10.2	9.7	5.0	3.3	0.35	0.34	—	—	—	—
S5	10.2	9.9	4.9	3.2	0.46	0.43	52.40	52.83	8.80	8.46

[a] *Theo = theoretical; **Exp = experimental.

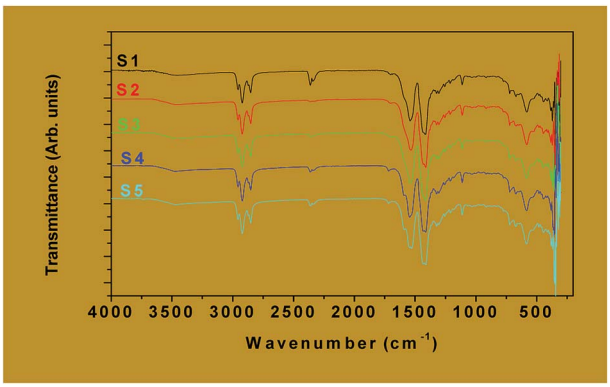

Fig. 2 FTIR spectra of the as-prepared samples S1 to S5.

Table 2 Characteristic FTIR absorption bands of samples S1 to S5 and their assignments[a]

Functional groups	Vibration mode	Wave number (cm^{-1})
O–H/H_2O	ν	3420
	δ	1536
O–H/Fe–OH	ν	3420
CH/CH_3	ν_{as}	2957
	ν_s	2872
CH/CH_2	ν_{as}	2923
	ν_s	2853
C–C	ν_{as}	920
OCO	ν_{as}	1581
	ν_s	1431
	δ	674
	π	641
$(CH_2)_6$	δ	1321
	ρ	723
Fe–O	ν	580
Cu/Co–O	ν	370

[a] ν: stretching (as: asymmetric; s: symmetric); δ: deformation in the plane; π: deformation outside the plane and ρ: wagging.

3.1.3. Thermogravimetric analysis (TGA). Fig. 3 shows the TGA curves for sample S2 (Fig. 3a) and comparative TGA curves for S1 to S5 (Fig. 3b). The TGA curve of sample S2 (Fig. 3a) selected as representative of all the samples presents two main weight loss steps. Step 1 (2.8% weight loss) occurs between ~50 °C and ~100 °C and corresponds to dehydration with the removal of 2 molecules of water of crystallization (*cf.* 3.3% theoretical weight loss). The Simultaneous Differential Thermal Analysis (DTA) curve shows that the dehydration step is endothermic. Step 2 (78.1% weight loss) occurring between 130 °C and 385.5 °C is attributable to the loss of 3 molecules of 7-pentadecanone ($C_{15}H_{30}O$), 1 molecule of water (H_2O) and 3 molecules of carbon dioxide (CO_2) with a combined theoretical weight loss of 75.4%. The DTA curve shows broad exothermic peaks indicating that the formation of the final product of decomposition is accompanied by energy losses. The total weight loss after decomposition is 80.9% (*cf.* 78.7% expected). The residue after decomposition is 19.1% which corresponds to copper-doped cobalt ferrite, $Co_{0.98}Cu_{0.02}Fe_2O_4$ (*cf.* 21.3% expected). These TGA results indicate that the precursor decomposes in air at a relatively low temperature (~380 °C) to give the copper-doped cobalt ferrite. The TGA curves (Fig. 3b) for S1 to S5 follow a similar pattern.[41]

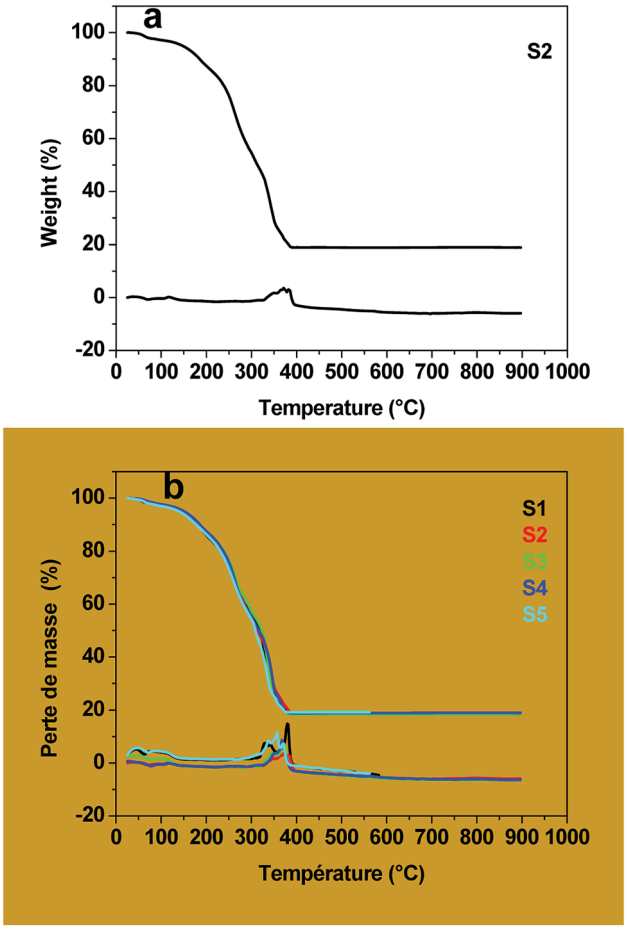

Fig. 3 TGA curves of the as-prepared samples S2 (a) and S1 to S5 (b).

3.2. Analysis of the decomposition products

3.2.1. FTIR analysis. The FTIR spectra of the products (S1P to S5P) obtained after the decomposition of samples S1 to S5 at 400 °C for 3 h are represented in the Fig. 4. All the spectra show only 2 absorption bands: at 540 cm^{-1} and 357 cm^{-1} corresponding to the metal–oxygen bonds, Fe–O and Cu/Co–O, respectively, which are in agreement with those reported in the literature.[42–45] The absence of other absorption bands is an indication that the decomposition of the precursors was complete at that temperature.

For spinel ferrites, the band appearing at the higher wave number (500–600 cm^{-1}) is usually assigned to tetrahedral coordination while that at the lower wave number (385–450 cm^{-1}) is often ascribed to octahedral coordination.[46,47] Thus, it can be concluded that the products, S1P to S5P, correspond to the cobalt ferrite spinel. Avazpour *et al.*[45] have obtained similar results with the absorption bands at 540 cm^{-1} and 331 cm^{-1} corresponding, respectively, to the tetrahedral and octahedral groups in cobalt ferrite.

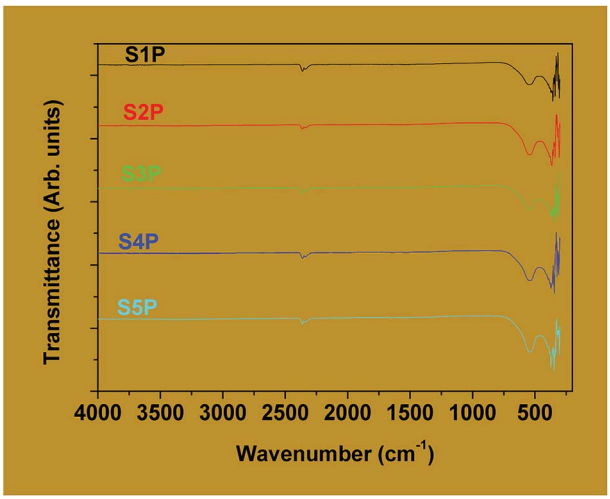

Fig. 4 FTIR spectra of the decomposition products S1P to S5P.

3.2.2. Structure and morphology. Fig. 5 shows the room temperature XRD patterns of the decomposition products S1P to S5P. These XRD patterns consist of diffraction peaks which are well indexed from the origin through the higher 2θ values to the crystal planes: (111), (220), (311), (222), (400), (422), (511), (440), (620) and (533) of the $CoFe_2O_4$ compound (JCPDS card no: 79-1744). This corresponds to a spinel structure, ($Fd\bar{3}m$ space group).[24] The lattice parameters "a" of all these samples are presented in Table 3. The parameter decreases from 8.352 Å to 8.344 Å as the doping percentage (x) increases from 0 to 0.04 but increases from 8.344 to 8.366 Å as x increases from 0.06 to 0.08. These variations are probably related to the structure of the compounds. The parent material ($CoFe_2O_4$) obtained through the coprecipitation method used in this work could be a mixed spinel structure where a part of Co(II) and Fe(III) ions are found in the tetrahedral and octahedral interstices occupied. For a copper content (x) less than 0.06, only the cobalt(II) ions of the tetrahedral sites are substituted. The unit cell parameter of the compound slightly decreases since the ionic radii of copper(II) and cobalt(II) ions are, respectively, 0.57 Å and 0.58 Å in a tetrahedral coordination.[48] But for a copper content greater than or equal to 0.06, all the copper ions of the tetrahedral site are substituted and a part of the cobalt(II) ions located in the octahedral sites are also replaced. The unit cell parameter of the compound, therefore, increases since the ionic radius of the copper(II) ion (0.73 Å) is greater than that of cobalt(II) (0.65 Å) in an octahedral coordination.[48]

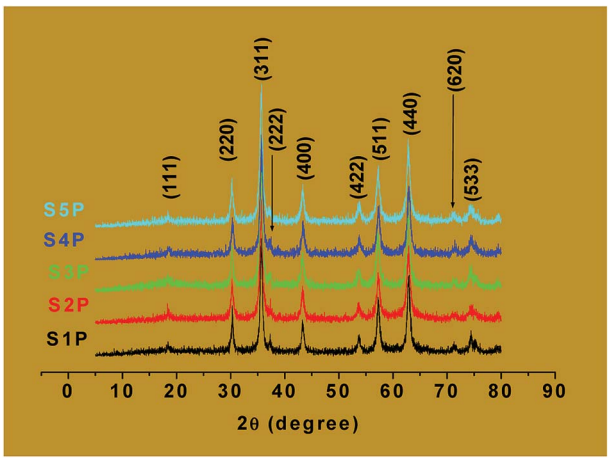

Fig. 5 Powder XRD patterns of the decomposition products S1P to S5P.

Table 3 Lattice parameter and average crystallite size of the decomposition products S1P to S5P

Samples	S1P	S2P	S3P	S4P	S5P
a (Å)	8.352	8.350	8.338	8.344	8.366
D (nm)	16.8	13.8	13.7	13.5	13.6

From the (311) diffraction line, the average crystallite diameters (D) of the samples (Table 3) were estimated using the Scherrer equation[5,49] and were found to decrease from 16.8 nm in the pure cobalt ferrite with increasing the copper content (x), to a value of 13.5 nm for $x = 0.06$. Between $x = 0.06$ and $x = 0.08$, however, the crystallite sizes increased to 13.6 nm. The observed decrease in crystallite size with doping up to $x = 0.06$ can be attributed to the substitution of cobalt(II) ions by the relatively smaller copper(II) ions in the tetrahedral site. The increase in size between $x = 0.06$ and $x = 0.08$ could be attributed to the fact that the substitution of the cobalt(II) ions by the relatively larger copper(II) ions rather takes place in the octahedral site, which is larger, thus, provoking an increase in the particle size. This phenomenon has been observed by other researchers for values of x higher than 0.08.[10,50] Furthermore, the crystallite sizes of the samples vary only slightly with increasing doping. This is normal since the doping levels are very low and the differences in doping concentrations are also very small. The closeness in these values is an indication that nano-sized particles of these materials have been obtained *via* the coprecipitation method employed.

The SEM images showing the morphology and microstructure of the decomposition products are as presented in Fig. 6 for the three (03) samples S1P (Fig. 6a), S3P (Fig. 6b) and S5P (Fig. 6c) while a further investigate on the morphology carried out by TEM is shown in Fig. 7 (S1P (Fig. 7a) and S2P (Fig. 7b)). The SEM images indicate that there is agglomeration and that the crystals are homogeneous, regular and yeast-like in shape. The particle sizes of about 20 nm estimated from TEM analysis are in good agreement with those (14 nm) deduced from XRD data. The phenomenon of agglomeration observed with these samples can be explained on the basis of their small particle sizes and the absence of steric hindrance both of which facilitate the particles coming together to form agglomerates. The very low agglomeration depicted by TEM analysis suggests that the critical coagulation concentration of the cobalt spinel ferrite samples correlates positively with the specific surface area. In other words, samples with higher specific surface areas are indicative of the fact that it is the surface chemistry rather than the bulk properties that are dominant in spinel ferrite aggregation.[51] This agglomeration phenomenon in the cobalt ferrites has also been reported in the literature.[28,31,36,52,53]

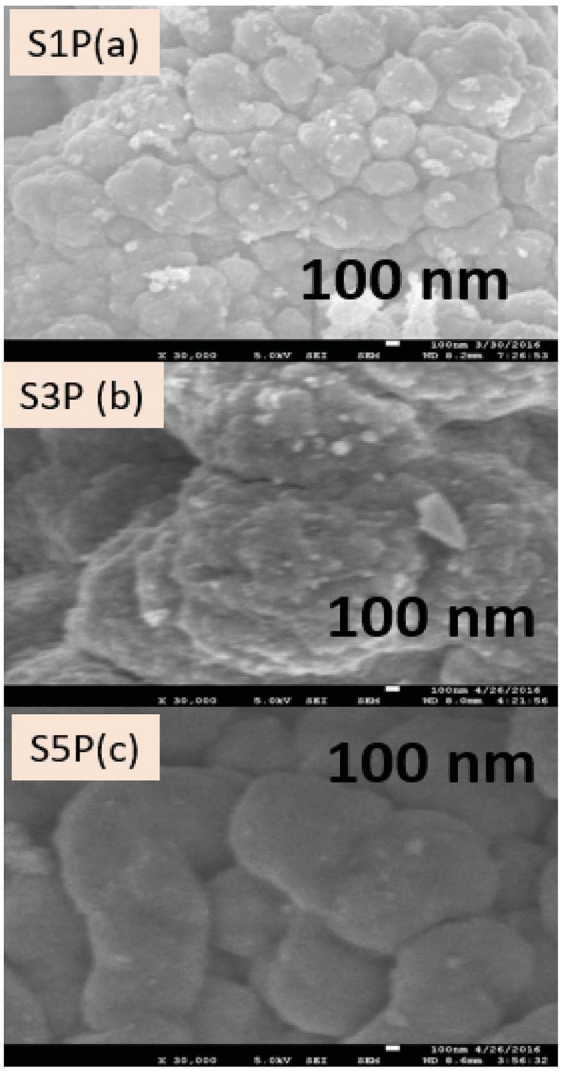

Fig. 6 SEM images of the decomposition products S1P (a), S3P (b) and S5P(c).

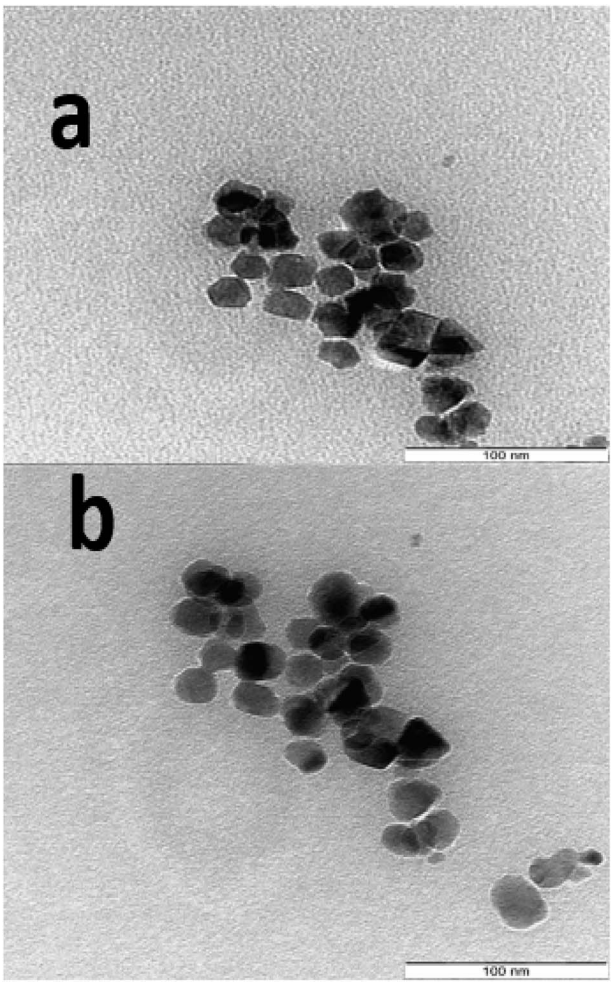

Fig. 7 TEM images of the decomposition products S1P (a) and S5P (b).

3.2.3. XPS analysis. The chemical state of the various constituents of the decomposition products S1P, S3P and S5P were investigated by XPS. The wide-scan XPS spectra of these samples in the binding energy range 200 to 965 eV, are presented in Fig. 8. The binding energies of the particles were calibrated by taking the C1s peak as reference (~285 eV). As expected, the XPS spectra showed that copper, cobalt, iron and oxygen are present in the samples. The broad peaks in the 830–930 eV region represent the Auger lines which are usually present in the XPS spectra.[54] They are assigned to the Fe LMM Auger lines. The XPS spectra given in Fig. 9 display binding energies which are assigned to Co2p (Fig. 9a), Cu2p (Fig. 9b) and Fe2p (Fig. 9c) on the surface of the $Co_{1-x}Cu_xFe_2O_4$ ferrites ($x = 0, 0.04, 0.08$).

The binding energies of Fe2p, Co2p and Cu2p are presented in Table 4. The binding energies of Cu $2p_{3/2}$ and Cu $2p_{1/2}$ for the samples S3P were obtained, respectively, as 932.6 eV and 952.4 eV while for S5P the values were, respectively, 932.7 eV and 952.4 eV (Fig. 9b and Table 4). This suggests the presence of Cu^{2+} as reported elsewhere.[55,56] Table 4 and Fig. 9a show that the average binding energy of Co $2p_{3/2}$ for S1P, S3P and S5P is about 780.4 eV while that of Co $2p_{1/2}$ is 795.4 eV for the same samples. Fig. 9c gives an average value of 710.9 eV for Fe $2p_{3/2}$ and 719 eV for Fe $2p_{1/2}$ for samples S1P, S3P and S5P. The results obtained in this work for Co and Fe have been ascribed to Co^{2+} and Fe^{3+} by other researchers.[57–60] The slight differences observed in the

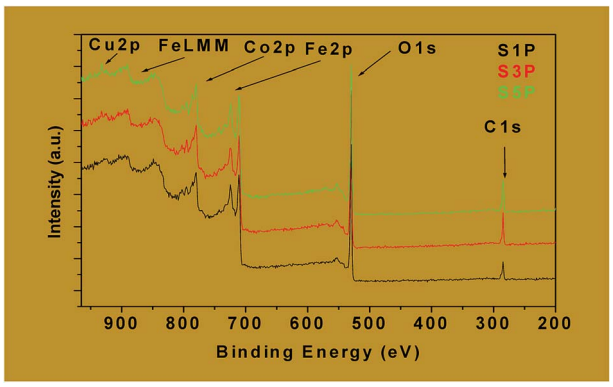

Fig. 8 Wide scan XPS spectra of the decomposition products S1P, S3P and S5P.

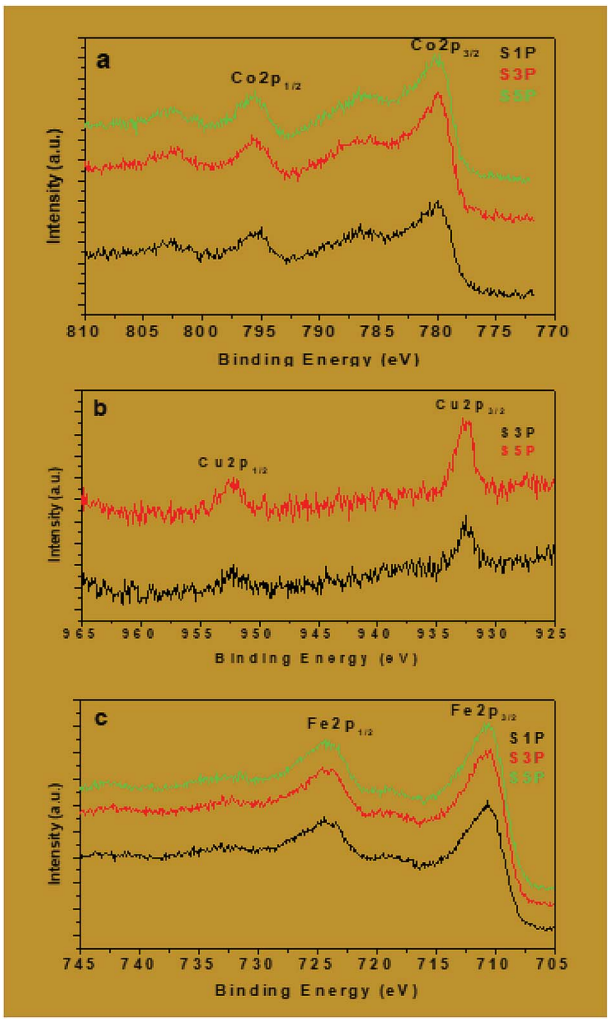

Fig. 9 Co2p (a), Cu2p (b) and Fe2p (c) XPS spectra of the decomposition products S1P, S3P and S5P.

Table 4 Binding Energies of Fe 2p, Co 2p and Cu 2p of the decomposition products S1P, S3P and S5P

	S1P	S3P	S5P
Fe $2p_{1/2}$	724.4	724.4	724.4
Fe $2p_{3/2}$	710.9	710.8	711
Co $2p_{1/2}$	795.3	795.4	795.5
Co $2p_{3/2}$	780.3	780.4	780.5
Cu $2p_{1/2}$	0.0	952.4	952.4
Cu $2p_{3/2}$	0.0	932.6	932.7

binding energies of Co and Fe in the three (03) samples, S1P, S2P and S3P, are most likely due to the change in their chemical environment provoked by the presence of the dopant (Cu). These differences could also be as a result of the formation of a mixed spinel as revealed by XRD. The fact that the characteristic peaks of Fe, Cu, Co, Cu^{+}, Co^{3+} and Fe^{2+} species are absent from the spectra, indicates that only Fe^{3+}, Co^{2+} and Cu^{2+} ions are present on the surface of the compounds and, thus, confirms the proposed formulation $Co_{1-x}Cu_xFe_2O_4$. The XPS results above are consistent with those of XRD for the decomposition products S1P, S2P and S5P, thus, confirming the formation of undoped and copper-doped cobalt ferrite structures and excluding the presence of any mixed phases of CuO, CoO and Fe_2O_3.

3.2.4. Magnetic properties. Room temperature magnetic hysteresis loops (M–H) of the nanocrystalline undoped and copper-doped cobalt ferrite ($Co_{1-x}Cu_xFe_2O_4$) powders are shown in Fig. 10. Magnetic parameters such as saturation magnetization (M_s), coercivity (H_c), remanent magnetization (M_r), magnetocrystalline anisotropy constant (K) and reduced magnetization (M_r/M_s) were obtained from the hysteresis loop. Since the magnetization is not saturated even at the highest field of measurement (60 kOe), saturation magnetization was calculated from the initial magnetization curve by plotting M *versus* $1/H$ and then extrapolating the magnetization to $1/H = 0$. The magnetocrystalline anisotropy constant (K) was calculated using the equation $K = \mu_0 M_s H_c \rho/2$ where the density ρ is given by $\rho = 8M/(N_A a^3)$ with N_A, the Avogadro's constant and, M and a, the molar weight and the lattice parameter of the sample, respectively. The different magnetic parameters are tabulated in Table 5. As can be observed from Table 5, M_s values for the as-synthesized samples increase from 67.1 to 73.5 emu g^{-1} (for x varying from 0 to 0.06) before decreasing to 68.5 emu g^{-1} with $x = 0.08$ (Fig. 11). The initial increase in M_s as x increases can be explained by the possible substitution of Co^{2+} by Cu^{2+} at the tetrahedral sites of the spinel ferrite lattice. These observed trends in the variation of M_s can be justified by Neel's two-sublattice magnetization model.[32,61,62] According to this model, magnetization (in μ_B) is given by $M\ (\mu_B) = M_B - M_A$, where M_A and M_B are the net magnetic moments of A (tetrahedral) and B (octahedral) sites, respectively. The magnetic moment of Cu^{2+} (1 μ_B) is less than that of Co^{2+} (3 μ_B). Thus, due to the substitution of Co^{2+} by Cu^{2+} at the tetrahedral sites, M_A decreases and the net magnetization, therefore, increases. At higher levels of substitution ($x = 0.08$) it is possible that part of Co^{2+} is substituted at the octahedral sites so that the net magnetization decreases due to the decrease in the value of M_B. These observations above confirm the results obtained by XRD analysis. Similar results have also been reported recently for Zn-

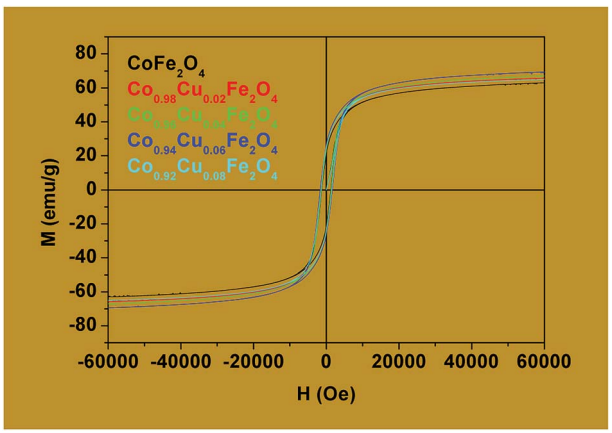

Fig. 10 Magnetic hysteresis loops of the ferrite samples S1P to S5P.

Table 5 Magnetic parameters of the decomposition products

Samples	H_c (Oe)	M_s (emu g^{-1})	M_r (emu g^{-1})	M_r/M_s	K (J m^{-3})
S1P	1284.9	67.1	21.2	0.32	0.023
S2P	1362.8	69.5	23.8	0.34	0.029
S3P	1377.9	71.1	23.5	0.33	0.026
S4P	1632.3	73.5	26.4	0.36	0.032
S5P	1544.5	68.5	25.2	0.37	0.028

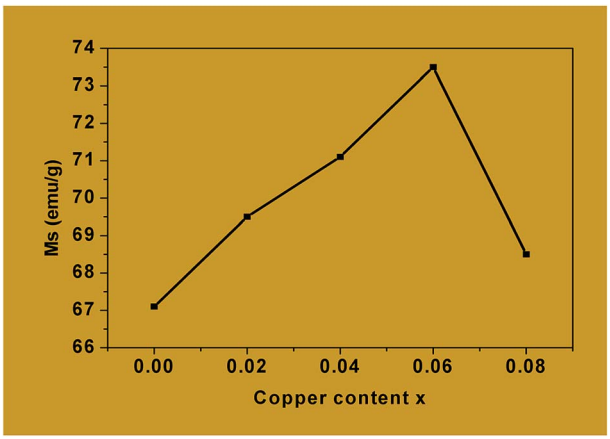

Fig. 11 Saturation magnetization M_s *versus* copper content x in $Co_{1-x}Cu_xFe_2O_4$.

doped cobalt ferrite.[63] This tendency of M_s increasing in $Co_{1-x}Cu_xFe_2O_4$ as x increases is being observed for the first time in this work since other researchers[10,22,24,64] have reported opposite trends. This difference can be explained on the basis of the fact that all the reported studies are performed with substitution intervals for $x \geq 0.1$ whereas in this work the level of substitution is below 0.1 ($x = 0$ to 0.08). To the best of our knowledge there are no reports in the literature at these very low levels of Cu^{2+} substitution in cobalt ferrites.

The values of M_s obtained for $Co_{1-x}Cu_xFe_2O_4$ are lower than for the bulk cobalt ferrite and this could be attributed to the very small size of the nanoparticles in the former. For example, the saturation magnetization, M_s, obtained for $x = 0$ is 67.1 emu g^{-1} which is much lower than that reported for the bulk cobalt ferrite ($\approx$90 emu g^{-1}).[65,66] Canting of spins at the surface of the particles and/or the magnetically dead layer at the surface of the particles is responsible for the observed lower value of magnetization.[66–69]

Table 5 also shows that the coercivity (H_c) increases from 1284.9 Oe to 1632.3 Oe as x is increased from 0 to 0.06 and then decreases to 1544.5 Oe for $x = 0.08$. The decrease in coercivity for $x = 0.08$ is being attributed to the replacement of Co^{2+} by Cu^{2+} from the octahedral sites. This, in turn, is responsible for the high magnetocrystalline anisotropy of cobalt ferrite, where the coercivity is related to the magnetocrystalline anisotropy constant through the relation $H_c = 2K/\mu_0 M_s$.[25] The small magnetic anisotropy of Cu^{2+} ions as compared to that of Co^{2+} ions reduces the magnetocrystalline anisotropy constant at higher levels of substitution.[70,71]

The values of M_r/M_s for copper-doped cobalt ferrites which vary from 0.32 to 0.37 are shown in Table 5. These values are less than the typical value of "1.0" expected for single domain isolated ferrimagnetic samples. The observed deviation from unity (1) could be attributed to the interactions between the grains which, in turn, are affected by the grain size distribution in the material.[29,72]

For $CoFe_2O_4$ ($x = 0$) obtained by calcining the precursor at 400 °C, the coercivity H_c is 1284.9 Oe (Table 5). This value is higher than that of 1100.72 Oe obtained by Samavati *et al.*,[36] heating at 800 °C and that of 1060.24 Oe obtained by Balavijayalakshmi *et al.*,[24] heating at 900 °C. These results clearly indicate that, for the same synthesis route, the processing temperature has an influence on the magnetic properties of the $CoFe_2O_4$ ferrite nanoparticles. This can be explained by the fact that by heating above 400 °C, the thermal energy is sufficient to allow the migration of Co^{2+} ions from the octahedral to the tetrahedral sites and the number of such Co^{2+} ions migrating increases with the processing temperature. This migration leads to a decrease in the magnetocrystalline anisotropy which, in turn, is responsible in the decrease of coercivity.[73] Another possible explanation is that the increase in the size of the particles when calcined at higher temperatures could cause a decrease in the coercivity.

All the results obtained in this work from the magnetic measurements for the materials ($Co_{1-x}Cu_xFe_2O_4$) indicate that they are ferromagnetic owing to the fact that, as can be observed from the hysteresis loops, the samples have a spontaneous magnetization even in the absence of an applied magnetic field. This, therefore, makes them potential candidates for various applications such as in biomedicine and in microwave devices. As far as applications in biomedicine are concerned, the samples obtained in this work have smaller sizes which are the predominant factors in the killing bacteria very fast.[23,36] In the same light, Samavati *et al.*[36] and Noppakun *et al.*[23] have synthesized

Table 6 Variation of particle sizes of $CoFe_2O_4$ with the method and temperature of synthesis

Powder obtained	Synthesis method	Decomposition temperature (°C)	Particle sizes (nm)	Saturation magnetization M_s (emu g^{-1})	Ref.
$CoFe_2O_4$ nanospheres	Coprecipitation (HO^- ligand)	800	32	61.06	36
$CoFe_2O_4$ nanoangles	Sol–gel	800	42.54	—	23
$CoFe_2O_4$ nanoplates	Coprecipitation (HO^- ligand)	900	37	72.06	24
$CoFe_2O_4$ nanospheres	Hydrothermal	140	40	86	44
$CoFe_2O_4$ nanospheres	Solvothermal	160	30	73	28
$CoFe_2O_4$ nanospheres	Coprecipitation (octanoate ion ligand)	400	20	67.1	This work

$Co_{1-x}Cu_xFe_2O_4$ (x = 0, 0.3, 0.5, 0.7, 1) by the coprecipitation method using hydroxide ion as ligand, for the former and by the sol–gel method using citric acid as chelating agent, for the latter. The groups obtained particle sizes varying from 30 nm to 20 nm and 42 nm to 38 nm, respectively, as the copper concentration was increased. They are all concluded that the smallest particles have the highest killing rate on the *E. coli* bacteria. With regards to microwave applications, G. P. Rodrigue[74] has showed that the ferrites are used in general in microwave devices. More precisely, they are used as signal amplitude limiters[75] and frequency multipliers[76] in microwave devices.

Table 6 shows a comparison of results from this work with those of other researchers with regards to the variation of particle sizes with the synthesis method and temperature.

4. Conclusion

We have successfully synthesized $Co_{1-x}Cu_xFe_2O_4$ nanoparticles *via* the pyrolysis of copper-cobalt-iron hydroxooctanoate prepared by coprecipitation at a relatively low temperature (~380 °C) and, for the first time, at very low dopant concentrations (x = 0, 0.02, 0.04, 0.06, 0.08). The particles obtained are crystalline and are of nanosize based on calculations using the Scherrer equation which gave crystallite sizes ranging between 14 and 17 nm and also from TEM analysis which showed a particle size of ~20 nm. Direct evidence for the presence of Cu in the cobalt ferrite crystal structure is provided by XPS which, combined with XRD, showed the formation of a single cubic mixed spinel structure in which a maximum value of x = 0.06 of copper is found in the tetrahedral sites and the remainder in the octahedral sites. VSM measurements confirm the above results obtained by XPS combined with XRD. VSM results also showed that the final materials are ferromagnetic and could be good candidates for various applications including in biomedicine and in microwave devices.

On the whole, the present results demonstrate that the coprecipitation synthesis technique used in this work is not only simple, low cost, controllable, reproducible and versatile but can also be applied to prepare a wide variety of target compounds with a good control of phase purity and stoichiometry.

Conflicts of interest

There are no conflicts to declare.

Acknowledgements

The authors sincerely thank Sophie Hermans, Pierre Eloy and Christelle Dzesse for the TGA, XPS and C, H analyses, respectively.

Notes and references

1 A. Godlyn Abraham, A. Manikandan, E. Manikandan, S. Vadivel, S. K. Jaganathan, A. Baykal and P. S. Renganathan, *J. Magn. Magn. Mater.*, 2018, **452**, 380–388.
2 A. Manikandan, A. Saravanan, S. Arul and M. Bououdina, *J. Nanosci. Nanotechnol.*, 2015, **15**, 4358–4366.
3 A. Manikandan and S. Arul Antony, *J. Supercond. Novel Magn.*, 2014, **27**, 2725–2733.
4 G. Padmapriya, A. Manikandan, V. Krishnasamy, S. K. Jaganathan and S. Arul Antony, *J. Supercond. Novel Magn.*, 2016, **29**, 2141–2149.
5 A. M. Ibrahim, M. M. A. El-latif and M. M. Mahmoud, *J. Alloys Compd.*, 2010, **506**, 201–204.
6 A. Azam, *J. Alloys Compd.*, 2012, **540**, 145–153.
7 J. Balavijayalakshmi, N. Suriyanarayanan, R. Jayaprakash and V. Gopalakrishnan, *Phys. Procedia*, 2013, **49**, 49–57.
8 I. H. Gul, A. Maqsood, M. Naeem and M. N. Ashiq, *J. Alloys Compd.*, 2010, **507**, 201–206.
9 S. Chakrabarty, A. Dutta and M. Pal, *J. Alloys Compd.*, 2014, **625**, 216–223.
10 D. M. Jnaneshwara, D. N. Avadhani, B. Daruka Prasad, H. Nagabhushana, B. M. Nagabhushana, S. C. Sharma, S. C. Prashantha and C. Shivakumara, *Spectrochim. Acta, Part A*, 2014, **132**, 256–262.
11 M. Sugimoto, *J. Am. Ceram. Soc.*, 1999, **82**, 269–280.
12 K. N. Trohidou, *Magnetic Nanoparticle Assemblies*, Pan Stanford, 1st edn, 2014.
13 A. Manikandan, J. Judith Vijaya and L. John Kennedy, *Phys. E*, 2013, **49**, 117–123.
14 D. Maruthamani, S. Vadivel, M. Kumaravel, B. Saravanakumar, P. Bappi, S. Sankar Dhar, A. Habibi-Yangjeh, A. Manikandan and G. Ramadoss, *J. Colloid Interface Sci.*, 2017, **498**, 449–459.
15 S. Asiri, M. Sertkol, S. Guner, H. Gungunes, K. M. Batoo, T. A. Saleh, H. Sozeri, M. A. Almessiere, A. Manikandan and A. Baykal, *Ceram. Int.*, 2018, **44**, 5751–5759.
16 G. Mathubala, A. Manikandan, S. Arul Antony and P. Ramar, *Nanosci. Nanotechnol. Lett.*, 2016, **8**, 375–381.
17 W. Bayoumi, *J. Mater. Sci.*, 2007, **42**, 8254–8261.
18 N. M. Deraz and A. Alarifi, *J. Anal. Appl. Pyrolysis*, 2012, **94**, 41–47.
19 A. Silambarasu, A. Manikandan and K. Balakrishman, *J. Supercond. Novel Magn.*, 2017, **30**, 2631–2640.
20 A. T. Ravichandran, J. Srinivas, R. Karthick, A. Manikandan and A. Baykal, *Ceram. Int.*, 2018, **44**, 13247–13252.
21 S. Rajmohan, V. Jeseentharani, A. Manikandan and J. Pragasam, *Nanosci. Nanotechnol. Lett.*, 2016, **8**, 393–398.
22 M. Hashim, Alimuddin, S. Kumar, B. H. Koo, S. E. Shirsath, E. M. Mohammed, J. Shah, R. K. Kotnala, H. K. Choi, H. Chung and R. Kumar, *J. Alloys Compd.*, 2012, **518**, 11–18.
23 N. Sanpo, J. Wang and C. C. Berndt, *J. Nano Res.*, 2013, **22**, 95–106.
24 J. Balavijayalakshmi, N. Suriyanarayanan and R. Jayapraksah, *Mater. Lett.*, 2012, **81**, 52–54.
25 K. Maaz, S. Karim, A. Mashiatullah, J. Liu, M. D. Hou, Y. M. Sun, J. L. Duan, H. J. Yao, D. Mo and Y. F. Chen, *Phys. B*, 2009, **404**, 3947–3951.
26 B. K. Bammannavar, L. R. Naik and R. B. Pujar, *Prog. Electromagnet. Res. Lett.*, 2008, **4**, 121–129.
27 D. Makovec and A. Kodre, *J. Nano Res.*, 2010, **12**, 1263–1273.
28 J. Ma, J. Zhao, W. Li, S. Zhang, Z. Tian and S. Basov, *Mater. Res. Bull.*, 2013, **48**, 214–217.

29 E. V. Gopalan, P. A. Joy, I. A. Al-omari, D. S. Kumar, Y. Yoshida and M. R. Anantharaman, *J. Alloys Compd.*, 2009, **485**, 711–717.
30 S. Prathapani, M. Vinitha, T. V Jayaraman and D. Das, *J. Appl. Phys.*, 2014, **115**, 17A502.
31 R. Tholkappiyan and K. Vishista, *Mater. Sci. Semicond. Process.*, 2015, **40**, 631–642.
32 C. Singh, S. Bansal, V. Kumar, K. B. Tikoo and S. Singhal, *RSC Adv.*, 2015, **5**, 39052–39061.
33 A. R. Carole Villette and P. Tailhades, *J. Solid State Chem.*, 1995, **117**, 64–72.
34 R. L. Fomekong, University catholic of Louvain Belgium/ University of Yaounde I Cameroon, Doctorate/PhD thesis, 2016.
35 R. Lontio, P. Kenfack, D. Magnin, S. Hermans, A. Delcorte and J. Lambi, *J. Solid State Chem.*, 2015, **230**, 381–389.
36 A. Samavati, M. K. Mustafa, A. F. Ismail and M. H. D. Othman, *Mater. Express*, 2016, **6**, 473–482.
37 J. Lambi, A. Nsehyuka, N. Egbewatt, L. Cafferata and A. Arvia, *Thermochim. Acta*, 2003, **398**, 145–151.
38 M. Adediran Mesubi, *J. Mol. Struct.*, 1982, **81**, 61–71.
39 R. Lenin and P. A. Joy, *J. Phys. Chem. C*, 2016, **120**, 11640–11651.
40 M. Popescu, C. Turta, V. Meriacre, V. Zubareva, T. Gutberlet and H. Bradaczek, *Thin Solid Films*, 1996, **274**, 143–146.
41 S. Mauchauffee, Université Paul Verlaine-Metz, Doctorate/ PhD thesis, 2007.
42 R. M. Mohamed, M. M. Rashad, F. A. Haraz and W. Sigmund, *J. Magn. Magn. Mater.*, 2010, **322**, 2058–2064.
43 H. A. Hamad, M. M. A. El-latif, A. B. Kashyout, W. A. Sadik and M. Y. Feteha, *Russ. J. Gen. Chem.*, 2014, **84**, 2205–2210.
44 L. Zhao, H. Zhang, Y. Xing, S. Song, S. Yu and W. Shi, *J. Solid State Chem.*, 2008, **181**, 245–252.
45 L. Avazpour, M. A. Zandi, M. R. Toroghinejad and H. Shokrollahi, *J. Alloys Compd.*, 2015, **637**, 497–503.
46 R. Fareghi-Alamdari, F. Zandi and M. H. Keshavarz, *RSC Adv.*, 2015, **5**, 71911–71921.
47 H. Kumar, J. P. Singh, R. C. Srivastava, P. Negi, H. M. Agrawal and K. Asokan, *J. Nanosci.*, 2014, **2014**, 1–10.
48 R. D. Shannon, *Acta Crystallogr.*, 1976, **32**, 751–767.
49 L. Yao, Y. Xi, G. Xi and Y. Feng, *J. Alloys Compd.*, 2016, **680**, 73–79.
50 M. Hashim, S. E. Shirsath, S. S. Meena, R. K. Kotnala, S. Kumar, P. Bhatt, R. B. Jotania and R. Kumar, *Mater. Chem. Phys.*, 2013, **141**, 406–415.
51 D. Zhou, Z. Ji, X. Jiang, D. R. Dunphy, J. BrinkerA and A. Keller, *PLoS One*, 2013, **8**, e81239.
52 Z. Gu, X. Xiang, G. Fan and F. Li, *J. Phys. Chem. C*, 2008, **112**, 18459–18466.
53 R. Lontio, J. Ngolui, G. Roland, P. Kenfack, H. M. T. Kamta, C. Ngnintedem and A. Delcorte, *J. Solid State Chem.*, 2016, **241**, 137–142.
54 J. F. Moulder, W. F. Stickle, P. E. Sobol and K. D. Bomben, *Handbook of X-ray Photoelectron Spectroscopy*, Perkin-Elmer Corporation, Minesota, United States of America, 1992.
55 Y. B. Yaolin Xu, J. Sherwood, Y. qin and R. A. Holler, *Nanoscale*, 2015, **7**, 12641–12649.
56 R. Jamatia, A. Gupta and A. Kumar, *ChemistrySelect*, 2016, **4**, 852–860.
57 Z. Gu, X. Xiang, G. Fan and F. Li, *J. Phys. Chem. C*, 2008, **112**, 18459–18466.
58 X. Yang, X. Wang and Z. Zhang, *J. Cryst. Growth*, 2005, **277**, 467–470.
59 P. M. Kouotou and Z. Tian, *Phys. Status Solidi A*, 2015, **212**, 1508–1513.
60 W. P. Wang, H. Yang, T. Xian and J. L. Jiang, *Mater. Trans.*, 2012, **53**, 1586–1589.
61 S. U. Bhasker and M. V. R. Reddy, *J. Sol-Gel Sci. Technol.*, 2015, 396–402.
62 S. Bhukal, T. Namgyal, S. Mor, S. Bansal and S. Singhal, *J. Mol. Struct.*, 2012, **1012**, 162–167.
63 T. Tatarchuk, M. Bououdina, W. Macyk, O. Shyichuk, N. Paliychuk, I. Yaremiy, B. Al-Najar and M. Pacia, *Nanoscale Res. Lett.*, 2017, **12**, 141.
64 S. Briceño, H. Del Castillo, V. Sagredo, W. Bramer-Escamilla and P. Silva, *Appl. Surf. Sci.*, 2012, **263**, 100–103.
65 F. Bensebaa, F. Zavaliche, P. L. Ecuyer, R. W. Cochrane and T. Veres, *J. Colloid Interface Sci.*, 2004, **277**, 104–110.
66 P. Jeppson, R. Sailer, E. Jarabek, J. Sandstrom, B. Anderson, M. Bremer and D. G. Grier, *J. Appl. Phys.*, 2006, **100**, 114324.
67 R. H. Kodama, *J. Magn. Magn. Mater.*, 1999, **200**, 359–372.
68 A. Beitollahi, R. Sani, Y. V Maksimov and I. P. Suzdalev, *NSTI-Nanotech.*, 2006, **1**, 431–434.
69 L. Ajroudi, N. Mliki, L. Bessa, V. Madigou and S. Villain, *Mater. Res. Bull.*, 2014, **59**, 1–49.
70 G. Baldi, D. Bonacchi, C. Innocenti, G. Lorenzi and C. Sangregorio, *J. Magn. Magn. Mater.*, 2007, **311**, 10–16.
71 S. Ammar, A. Helfen, N. Jouini, F. Fiévet, I. Rosenman, F. Villain, P. Molinie and M. Danot, *J. Mater. Chem.*, 2001, **111**, 86–192.
72 S. Ayyappan, S. Mahadevan, P. Chandramohan, M. P. Srinivasan, J. Philip and B. Raj, *J. Phys. Chem. C*, 2010, **114**, 6334–6341.
73 P. Tailhades, C. Villette and A. Rousset, *J. Solid State Chem.*, 1998, **141**, 56–63.
74 G. P. Rodrigue, *J. Appl. Phys.*, 1969, **40**, 929–937.
75 R. W. Degrasse, *J. Appl. Phys.*, 1959, **30**, 1555.
76 W. P. Ayres, P. H. Vartanian and J. L. Melchor, *J. Appl. Phys.*, 1956, **27**, 188–189.